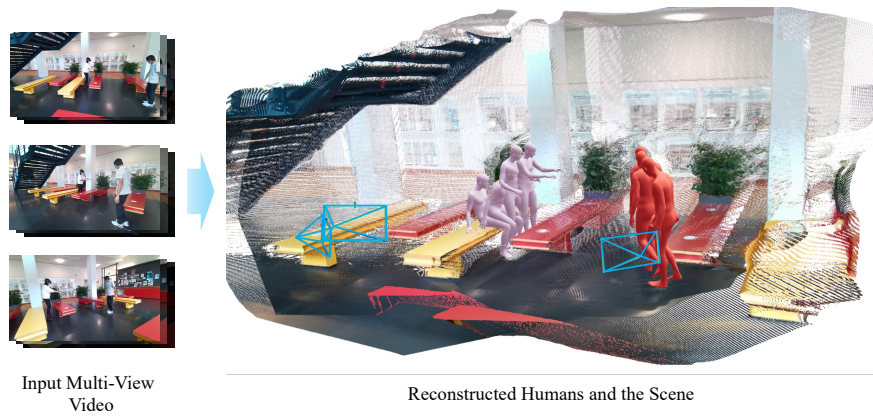


# Coherent Human-Scene Reconstruction from Multi-Person Multi-View Video in a Single Pass

Sangmin Kim<sup>1\*</sup>, Minhyuk Hwang<sup>1</sup>, Geonho Cha<sup>2</sup>, Dongyoon Wee<sup>2</sup>, and Jaesik Park<sup>1†</sup>

<sup>1</sup> Seoul National University  
<sup>2</sup> NAVER Cloud



**Fig. 1:** Given multi-person, multi-view videos, our proposed approach, **CHROMM**, reconstructs cameras, scene point cloud, and human meshes in a single pass.

**Abstract.** Recent advances in 3D foundation models have led to growing interest in reconstructing humans and their surrounding environments. However, most existing approaches focus on monocular inputs, and extending them to multi-view settings requires additional overhead modules or preprocessed data. To this end, we present CHROMM, a unified framework that jointly estimates cameras, scene point clouds, and human meshes from multi-person multi-view videos without relying on external modules or preprocessing. We integrate strong geometric and human priors from Pi3X and Multi-HMR into a single trainable neural network architecture, and introduce a scale adjustment module to solve the scale discrepancy between humans and the scene. We also introduce a multi-view fusion strategy to aggregate per-view estimates into a single representation at test-time. Finally, we propose a geometry-based multi-person association method, which is more robust than appearance-based approaches. Experiments on EMDB, RICH, EgoHumans, and EgoExo4D show that CHROMM achieves competitive

\* This work was done during an internship at NAVER Cloud.

† Corresponding author.

performance in global human motion and multi-view pose estimation while running over  $8\times$  faster than prior optimization-based multi-view approaches. Project page: <https://nstar1125.github.io/chromm>.

**Keywords:** Human-Scene Reconstruction · Multi-View · Multi-Person · Optimization-Free

## 1 Introduction

Reconstructing our surrounding environments in 3D is a fundamental problem in computer vision and graphics. In particular, modeling human motion and its surrounding environment is a challenging yet important task. Recovering humans and the scene in 3D can be applied to many downstream tasks such as robotics [1, 6, 11], autonomous driving [7, 9, 15, 44], and AR/VR [23, 36, 41].

Previous work [3, 47, 50] has focused either on reconstructing humans in a world coordinate system or on recovering static backgrounds. With advances in 3D foundation models such as DUSt3R [50] and VGGT [47], many works have sought to jointly recover humans and their environments by combining 3D foundation models with global human pose estimation models. Building on this line of work, recent approaches such as UniSH [25] and Human3R [8] unify human and scene reconstruction into a single feed-forward architecture. However, these methods operate on monocular inputs. Other works, such as HSfM [33] and HAMSt3R [37], have attempted to extend the setting to multi-view scenarios, but these approaches incur additional overhead, such as a 2D key-point estimator or cross-view re-identification modules. Such requirements introduce additional computational cost and system complexity, which may hinder their applicability in real-world scenarios.

To this end, we present CHROMM (Coherent **H**uman-Scene **R**ec**O**nstruction from **M**ulti-Person, **M**ulti-View Video), a unified framework that jointly reconstructs multiple humans and their surrounding environments from multi-view videos (Fig. 1). Our model does not require external modules such as 2D keypoint detectors or bounding box detectors, and preprocessed data such as cross-view person identities. A key challenge of data-driven human-scene reconstruction is the lack of large-scale datasets for supervision. Therefore, we leverage strong geometric and human priors from Pi3X [51] and Multi-HMR [3] by integrating them into a single unified framework. However, Pi3X predicts scene geometry at an approximate metric scale, leading to a scale mismatch with metric-scale SMPLs. To address this issue, we compute the head-pelvis length for humans in the image and compare it with that of the projected SMPLs. By computing the ratio of these two head-pelvis lengths, we can adjust the predicted scene scale for seamless integration.

To aggregate per-view human estimates into a coherent global representation in a single pass, we introduce a test-time optimization-free multi-view fusion strategy. We decompose human features into view-invariant and view-dependent components and fuse them separately. Attributes such as canonical-space pose

and body shape are shared across views, so we directly fuse the predicted parameters. In contrast, view-dependent attributes, such as rotation and translation, vary with the viewpoint. We therefore transform these predictions into a world coordinate system and explicitly compute the corresponding attributes in a shared world coordinate system.

Also, accurate cross-view person identities are essential to correctly fuse multiple humans across views. As mentioned above, prior work [33, 37] typically assumes that such identity information is provided before inference. Moreover, appearance-based re-identification methods [26] often struggle in scenarios where individuals are visually similar, such as people wearing uniforms, leading to unreliable associations. To address this issue, we introduce a multi-person association method that leverages explicit geometric cues, such as estimated 3D positions and human poses, to robustly associate individuals across views.

Experiments on EMDB [20], RICH [19], EgoHumans [22], and EgoExo4D [17] demonstrate that our model achieves competitive performance in both global human motion estimation and multi-view human pose estimation tasks. Moreover, compared with other optimization-based multi-view approaches, our model runs more than  $8\times$  faster while maintaining comparable reconstruction accuracy. To the best of our knowledge, CHROMM is the first unified framework that jointly reconstructs cameras, scenes, and humans from multi-person multi-view videos without external modules, preprocessing, or optimization.

Our main contributions are summarized as follows:

- We present CHROMM, the first unified framework that jointly reconstructs cameras, scenes, and humans from multi-person multi-view videos in a single pass without using external modules or preprocessed data.
- To handle the scale gap between Pi3X and SMPLs, we propose a scale adjustment module that utilizes head-pelvis length for scale refinement.
- We introduce a test-time multi-view fusion strategy that aggregates per-view estimates into a coherent global representation.
- We propose a multi-person association method that establishes cross-view person identity correspondences by using explicit geometric cues such as 3D positions and human poses.
- Experiments demonstrate that our model achieves competitive performance on global human motion estimation and multi-view human pose estimation tasks, while providing over  $8\times$  speedup compared to other optimization-based multi-view approaches.

## 2 Related Work

### 2.1 3D Scene Reconstruction

Classical 3D reconstruction approaches such as Structure-from-Motion (SfM) [4, 12, 30, 38, 45] and Multi-View Stereo (MVS) [13, 39, 40] estimate camera poses and scene geometry through feature matching and bundle adjustment. While

highly accurate, these optimization-based pipelines are computationally expensive and struggle in dynamic scenes. Recent data-driven approaches replace iterative optimization with feed-forward neural architectures. DUS<sub>t</sub>3R [50] predicts a 3D point map from an image pair in the coordinate system of the first camera, enabling efficient reconstruction, and MAS<sub>t</sub>3R [24] improves matching stability and reconstruction accuracy. VGGT [47] further replaces explicit camera estimation with direct network prediction, while Pi3 [51] introduces a permutation-equivariant architecture to improve robustness. More recent works, such as MapAnything [21] and Depth Anything 3 [27], extend these models toward metric-scale prediction. In this work, we build upon Pi3X, an extension of Pi3 that enables approximate metric-scale scene reconstruction, forming the basis of our unified human–scene modeling framework.

## 2.2 Human Mesh Recovery

Meanwhile, Human Mesh Recovery (HMR) has developed to predict the parameters of parametric human body models such as SMPL [31] and SMPL-X [35] from images. HMR2.0 [16] first introduced transformer-based modeling to HMR, leading to substantial performance improvements. Building upon this progress, Multi-HMR [3] enables multi-person whole-body reconstruction within a unified framework. In addition, it solves the problem in a single-shot manner, eliminating the need for bounding box detection. Recently, SAM-3D Body [53] has demonstrated strong performance 3D human mesh recovery from large-scale training.

While these methods primarily operate in the camera coordinate frame, recent research has shifted toward reconstructing humans in the world coordinate system. SLAHMR [54] decouples camera and human motion to recover globally aligned trajectories from monocular video. WHAM [43] improves world-grounded motion estimation through motion priors and contact-aware refinement. GVHMR [42] introduces a gravity-aligned intermediate coordinate system to stabilize world-space motion prediction. TRAM [52] combines SLAM-based camera estimation with transformer-based motion regression to reconstruct metric-scale human trajectories in world coordinates. These approaches enable world-grounded human motion reconstruction from monocular video. However, they focus on human trajectories and do not explicitly model the surrounding scene geometry.

## 2.3 Human-Scene Reconstruction

Recent work attempts to bridge global human pose estimation with 3D foundation models to jointly reconstruct humans and their surrounding environments. JOSH [29] reconstructs humans and scenes from monocular videos using foot-contact cues for global alignment, and its extension JOSH3R further adopts a feed-forward architecture. UniSH [25] integrates Pi3 and CameraHMR [25] based backbone with AlignNet for improved human-scene alignment, while Human3R [8] leverages CUT3R [48] to enable unified multi-person reconstruction with online inference. However, these approaches operate in monocular settings.

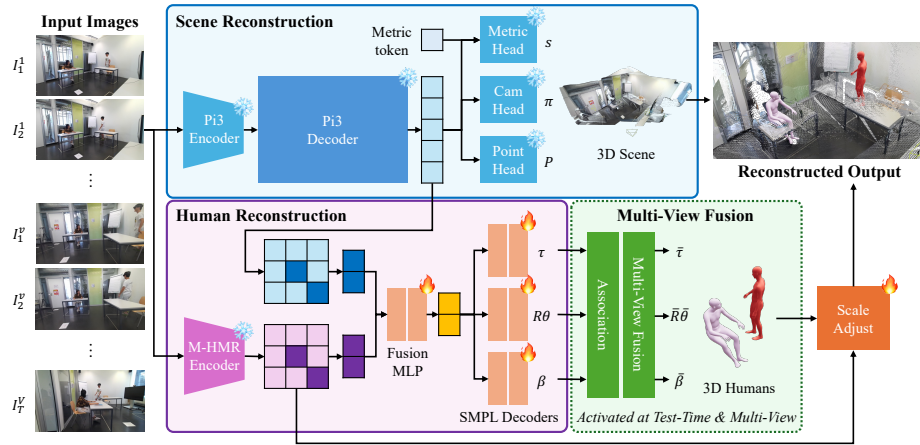


**Fig. 2: Overview of our pipeline.** Each frame is encoded by the Pi3 encoder and the Multi-HMR encoder. The Pi3 features are decoded to reconstruct the scene. Head tokens detected from Multi-HMR features are fused with the corresponding tokens from the Pi3 decoder tokens to predict SMPL parameters. At test time, we associate persons across views and fuse them into a global representation, followed by a scale adjustment module to align humans and the scene.

Several works also explore multi-view human-scene reconstruction. HSfM [33] estimates cameras, scenes, and human meshes while calibrating camera poses using human joints as correspondences, and HAMSt3R [37] jointly predicts segmentation, dense pose, and scene geometry in a feed-forward manner. However, these approaches operate on single frames and do not model human motion. Nevertheless, these methods rely on iterative optimization, external modules, and assume known cross-view person identities, resulting in higher computational cost and system complexity. In contrast, our model adopts a unified framework that jointly reconstructs cameras, scenes, and multiple humans from multiple views in a single pass without relying on external modules or preprocessed data.

### 3 Method

We present CHROMM, a unified network designed to jointly reconstruct human meshes, scene point clouds, and camera parameters from multi-person multi-view videos in a single-pass. Given RGB input images  $\{I_t^v\}_{t=1..T}^{v=1..V}$  consisting of  $V$  views and  $T$  timesteps per view, our model estimates the following for each view  $v$  and timestep  $t$ : (i) camera-space point map  $P_t^v$ , (ii) camera parameters  $\pi_t^v$ , and (iii) global SMPL-X parameters of  $M$  individuals that are shared across views. For each timestep  $t$  and person  $m$ , we represent the human state as  $(\bar{\theta}_t^m, \bar{\beta}_t^m, \bar{R}_t^m, \bar{\tau}_t^m)_{t=1..T}^{m=1..M}$  where  $\bar{\theta}_t^m \in \mathbb{R}^{52 \times 3}$  denotes the pose parameters in canonical space including body, left hand, right hand, and jaw,  $\bar{\beta}_t^m \in \mathbb{R}^{10}$  the

shape parameters,  $\bar{R}_t^m \in SO(3)$  the global root rotation, and  $\bar{\tau}_t^m \in \mathbb{R}^3$  the global 3D head position.

### 3.1 Model Architecture

Our model builds upon Pi3X [51], a 3D foundation model capable of predicting approximate metric-scale geometry. For human modeling, we adopt SMPL-X [35], a parametric human body model that can be controlled with the pose parameter  $\theta$  and the body shape parameter  $\beta$ . An overview of the pipeline is illustrated in Fig. 2.

**Dual-Feature Encoding.** We first flatten the multi-view video frames  $\{I_t^v\}_{t=1..T}^{v=1..V}$  into a single sequence  $\{I_n\}_{n=1..N}$ , where  $N = T \times V$ . Since Pi3 architecture is permutation-equivariant, we can successfully reconstruct the scene regardless of the input ordering. Given an input image  $I_n$ , our model first extracts two feature representations, (i) a scene-wise feature  $F_n^{scene}$  and (ii) a human-wise feature  $F_n^{human}$ . While the Pi3X encoder effectively captures global 3D geometry of the scene, it is not specifically optimized for detailed human geometry. Following [8], we adopt an additional encoder from Multi-HMR [3], which has been trained specifically for human representation. This dual-encoder structure allows the model to precisely estimate both scene-level geometry and detailed human motion.

Next, scene features  $\{F_n^{scene}\}_{n=1..N}$  are partitioned into patch tokens and fed into the Pi3X decoder with the register tokens, and processed through alternating attention layers. In contrast, the human features  $\{F_n^{human}\}_{n=1..N}$  bypass the Pi3X decoder and are directly passed to the human reconstruction head. Unlike Human3R [8], we intentionally avoid early fusion between the two feature tokens, as altering the decoder’s input distribution, even with frozen weights, negatively affects geometric reconstruction performance.

**Scene Reconstruction.** After the scene tokens are processed by the decoder, the decoded scene tokens are fed to the camera head and the point head to regress per-frame camera parameters  $\pi_n$  and local 3D point maps  $P_n$ , respectively. Unlike the original Pi3 model, which focuses on reconstructing scale-invariant geometry, Pi3X introduces a metric decoder to reconstruct the scene at near-metric scale. A metric token cross-attends to the decoded scene tokens and estimates a global scale factor  $s \in \mathbb{R}$ . This predicted scene scale  $s$  is applied to the local point maps and camera translations across all frames, enabling approximately metric-scale scene reconstruction. The decoded scene tokens are reshaped into feature maps  $\{\bar{F}_n^{scene}\}_{n=1..N}$ , which are passed to the human reconstruction head.

Since we only need the static scene point cloud, we exclude dynamic human regions from the predicted 3D points. We predict a dense human mask  $\mathcal{M}_n^{human}$  using a mask MLP that takes the human feature map  $F_n^{human}$  as input. The mask is produced with a sigmoid activation followed by pixel shuffle, and is subsequently applied to the local 3D point map  $P_n$  to filter out human regions.

**Human Reconstruction.** Following [8], for each frame  $n$ , we detect patches containing human heads from the human-wise feature and collect the corre-

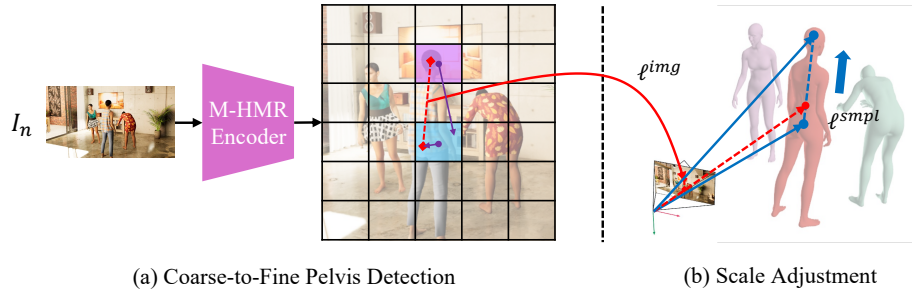


**Fig. 3: (Left)** Pelvis location is predicted in a coarse-to-fine manner. **(Right)** Scale is adjusted using the head–pelvis length ratio between the image and projected SMPL.

sponding human tokens as  $Z_n^{\text{human}} = \{F_{n,i,j}^{\text{human}} \mid (i, j) \in \mathcal{U}_n\}$ , where  $(i, j)$  denotes the spatial patch indices in the human feature map, and  $\mathcal{U}_n \subset \{1..h_h\} \times \{1..w_h\}$  is the set of detected head patch indices for frame  $n$ . For each detected head, we sample the corresponding tokens from the decoded scene feature map as  $Z_n^{\text{scene}} = \{F_{n,i',j'}^{\text{scene}} \mid (i', j') \in \mathcal{U}'_n\}$ , where  $(i', j') \in \mathcal{U}'_n$  denotes the corresponding patch indices in the scene feature map. The sampled tokens from the scene and human feature are fused through an MLP to produce human tokens  $H_n = \text{MLP}_{\text{fuse}}([Z_n^{\text{scene}} \mid Z_n^{\text{human}}])$ , where each token corresponds to an individual human in frame  $n$ . Each human token  $H_n^m$  is then fed into SMPL decoders, which regress the following SMPL parameters  $(\theta_n^m, \beta_n^m, R_n^m)$  using two-layer MLPs.

To consistently place each reconstructed human within the scene, we estimate the translation  $\tau_n^m$  of the 3D head joint in the camera coordinate system, as the human head is one of the most distinctive and consistently visible body parts in the image. Instead of directly regressing the 3D head translation as in [8], we reformulate translation estimation as a depth prediction problem. Following [3], we first predict the 2D head keypoint  $(u, v)_n^m$  in the image plane using an offset MLP. Given the predicted camera intrinsics  $K_n \in \mathbb{R}^{3 \times 3}$ , the 3D head translation  $\tau_n^m \in \mathbb{R}^3$  can be recovered by unprojecting the 2D head location with the estimated depth  $d_n^m \in \mathbb{R}$ .

Since the point head provides a strong depth prior, we can reformulate the depth estimation formulation above. Specifically, as the point head predicts a dense 3D point map  $P_n$ , we can obtain the depth map  $D_n$  from its z-coordinate. As the human head joint lies slightly behind the corresponding head region in the depth map, we reformulate the task as predicting a depth residual with respect to the sampled coarse depth  $d_{n,m}^{\text{coarse}}$  from  $D_n$ , instead of learning the head depth  $d_n^m$  directly. The final 3D head position is defined as follows:

$$d_n^m = d_{n,m}^{\text{coarse}} + \Delta d_n^m, \quad \tau_{n,m}^{\text{head}} = d_n^m K_n^{-1} [u_n^m \ v_n^m \ 1]^\top. \quad (1)$$

This reformulation stabilizes training and improves generalization beyond the training distribution.

**Scale Adjustment.** After reconstructing the scene point cloud and human meshes, we integrate them into a unified 3D representation. Thanks to the depth-

map-based translation defined in Eq. 1, the SMPL head joints are precisely positioned within the scene. However, Pi3X estimates the scene at a *near-metric* scale, which may cause misalignment with the metric-scale SMPL meshes. If the predicted scene scale  $s$  is underestimated, SMPL meshes may penetrate the ground, and if overestimated, they may float above it.

To address this issue, we propose a scale-adjustment module based on the average ratio between the head-pelvis distance observed in the image and that of the projected SMPL mesh. We select the pelvis as a stable body reference, since it remains relatively invariant to pose changes. To compute the image head-pelvis length, we localize the pelvis corresponding to each detected head. We reuse the detected head tokens  $Z_n^{\text{human}}$  from the human-wise feature  $F_n^{\text{human}}$  to locate the corresponding pelvis. However, directly predicting the pelvis location is challenging due to the larger spatial variation. Therefore, we adopt a coarse-to-fine pelvis detection strategy, as illustrated in Fig. 3.

Since each head token interacts with other patch tokens through self-attention in the Multi-HMR encoder, it encodes contextual information of the full body. We first use the head token to estimate a coarse pelvis location. Using the sampled patch from that location, we refine the pelvis position by predicting a local offset within the patch. If the person is partially cropped and the pelvis lies outside the image boundary, we use the coarse pelvis prediction estimated from the head token.

Using the detected 2D head and pelvis keypoints and the projected SMPL joints, we compute the image head-pelvis length  $\ell^{\text{img}}$  and SMPL head-pelvis length  $\ell^{\text{smpl}}$  per person as follows:

$$\ell^{\text{img}} = \|p^{\text{head}} - p^{\text{pelvis}}\|_2, \quad \ell^{\text{smpl}} = \|\mathcal{J}_{2\text{D}}^{\text{head}} - \mathcal{J}_{2\text{D}}^{\text{pelvis}}\|_2, \quad (2)$$

where  $p$  denotes the detected 2D keypoint and  $\mathcal{J}_{2\text{D}}$  the projected SMPL joint.

We then compute the global scale adjustment ratio by averaging the per-person ratios across all frames and individuals as,

$$r = \frac{1}{|\mathcal{S}|} \sum_{(n,m) \in \mathcal{S}} \frac{\ell_{n,m}^{\text{smpl}}}{\ell_{n,m}^{\text{img}}}, \quad (3)$$

where  $\mathcal{S}$  denotes the set of valid frame-person pairs. Finally, we obtain adjusted metric scale  $s^*$  by multiplying the global ratio to the predicted metric scale as  $s^* = r \cdot s$ , enabling consistent integration between the reconstructed scene and SMPL meshes.

### 3.2 Multi-View Fusion

To reconstruct humans from multi-view inputs, previous approaches typically employ multi-stage pipelines, such as detecting 2D poses and optimizing the human poses by minimizing reprojection error. Such procedures require external modules and additional optimization stages, increasing overall system complexity and computational cost. In this section, we introduce a test-time multi-view

fusion strategy that aggregates per-view estimates into a coherent human representation without relying on additional modules or optimization. We observe that the predicted human representation consists of view-invariant and view-dependent components. Based on this observation, we decompose the representation into these two categories and handle them separately.

**View-Invariant Components.** Among the predicted SMPL parameters, the shape parameter  $\beta$  is view-invariant, as it represents the body shape of an individual. Similarly, the pose parameters  $\theta$  in canonical space are consistent across views. To fuse these view-invariant components, we first group humans corresponding to the same individual across different views. For each grouped individual, we then compute the fused shape parameter  $\bar{\beta}$  and  $\bar{\theta}$  as the mean of the per-view predictions. We observe that explicitly averaging the parameters led to a performance gain compared to implicit human token max-pooling. We hypothesize that token-level pooling mixes view-dependent features, which degrades the estimation of view-invariant SMPL parameters.

**View-Dependent Components.** In contrast, the root rotation  $R$  and 3D head translation  $\tau$  are view-dependent, as they are predicted in each view’s camera coordinate system. To fuse components defined in separate spaces, we first transform all predicted root rotations and head translations into a shared world coordinate system using the estimated camera extrinsics. Next, we convert the global root rotation into quaternion form to ensure stable averaging. To compute the global 3D head position, rather than averaging per-view head translations, we calculate the global 3D head position via multi-view ray triangulation to enforce multi-view consistency. By considering the characteristics of each feature component, our fusion strategy leads to more precise performance improvements.

### 3.3 Multi-Person Association

To perform multi-view fusion, cross-view identity correspondence between individuals is required. Previous approaches [33, 37] either rely on external re-identification (ReID) modules or assume that identity information is explicitly provided. Such dependencies increase system complexity and computational overhead. Moreover, appearance-based ReID methods [26] often struggle in scenarios where individuals are visually similar, such as people wearing uniforms, leading to unreliable associations. To address this limitation, we propose a multi-person association method that leverages geometric cues, including human pose and global 3D position, to establish robust cross-view identity correspondence.

**Tracking.** Before performing cross-view association, we first track humans in each view using the detected head tokens  $Z_n^{\text{human}}$  from the human-wise feature  $F_n^{\text{human}}$ . These tokens capture person-specific contextual representations, enabling tracking to be formulated as a feature-matching problem across consecutive time steps. Following [8], we compute pairwise L2 distances between tokens and solve a one-to-one assignment. Unmatched detections are handled via an optimal transport [14] with a dustbin entry, which is solved using the Sinkhorn algorithm [10], ensuring stable tracklet maintenance.

To further stabilize per-view tracking, we filter out outlier estimates by comparing the estimated global 3D human joints between consecutive time steps for a tracked person. If temporal displacement exceeds a threshold, the corresponding match is considered an outlier and removed from the tracklet. This temporal filtering suppresses erroneous estimation, such as identity switches caused by occlusions or abrupt token mismatches.

**Association.** After per-view tracking, we perform cross-view multi-human association based on the resulting tracklets and assign global human identities. We first construct a view connectivity graph using k-nearest neighbors based on the average camera centers of each view. For each connected view pair, we compute pairwise matching scores between all human tracklets.

For each selected view pair, we evaluate a matching cost between tracklets over their overlapping frames. The cost consists of (i) a position term computed from global 3D joints, and (ii) a pose term computed from canonical-space joints, where both the root rotation and root translation are set to zero to obtain root-relative joint positions. We define the matching cost as,

$$\mathcal{C}(a, b) = \frac{1}{|\mathcal{T}_{a,b}|} \sum_{t \in \mathcal{T}_{a,b}} \frac{1}{J} \sum_{j=1}^J \left( \lambda_p \|\mathcal{J}_{t,j}^a - \mathcal{J}_{t,j}^b\|_2 + \lambda_\theta \left\| \mathcal{J}_{t,j}^{a,\text{canon}} - \mathcal{J}_{t,j}^{b,\text{canon}} \right\|_2 \right), \quad (4)$$

where  $\mathcal{T}_{a,b}$  denotes the set of overlapping timesteps between tracklets  $a$  and  $b$ , and  $\mathcal{J}^{\text{canon}}$  the root-aligned canonical joints. The weights  $\lambda_p$  and  $\lambda_\theta$  are set as 0.8 and 0.2, respectively. By combining both position and pose cues, the matching cost benefits from the robustness of 3D positional consistency while allowing pose similarity to resolve edge cases where position alone is insufficient.

We apply Hungarian matching to the cost matrix to obtain one-to-one assignments, and retain only matches whose cost is below a predefined threshold. After pairwise cross-view matching, we assign global human identities by merging matched tracklets across views. Details are provided in the supplement.

### 3.4 Training CHROMM

We train CHROMM in two stages. The first stage consists of learning human reconstruction, while the second stage focuses on predicting pelvis location.

**Stage 1 training.** In the first stage, we freeze the Pi3X backbone and the Multi-HMR encoder, and train the SMPL decoders together with the fusion, mask, and pelvis detection MLPs using the BEDLAM dataset [5]. Following [51], we align the predicted outputs to the ground-truth using a scale factor  $s_{\text{opt}}$  computed by a RoE solver [49]. We supervise the model using a combination of geometric losses that compare SMPL outputs with ground-truth SMPLs, parameter losses that directly compare SMPL parameters, and classification losses, including mask supervision, head, and pelvis detections. Details are provided in the supplement.

**Stage 2 training.** In the second stage, we unfreeze only the pelvis detection MLPs introduced in Sec. 3.1, while keeping all other modules fixed. We

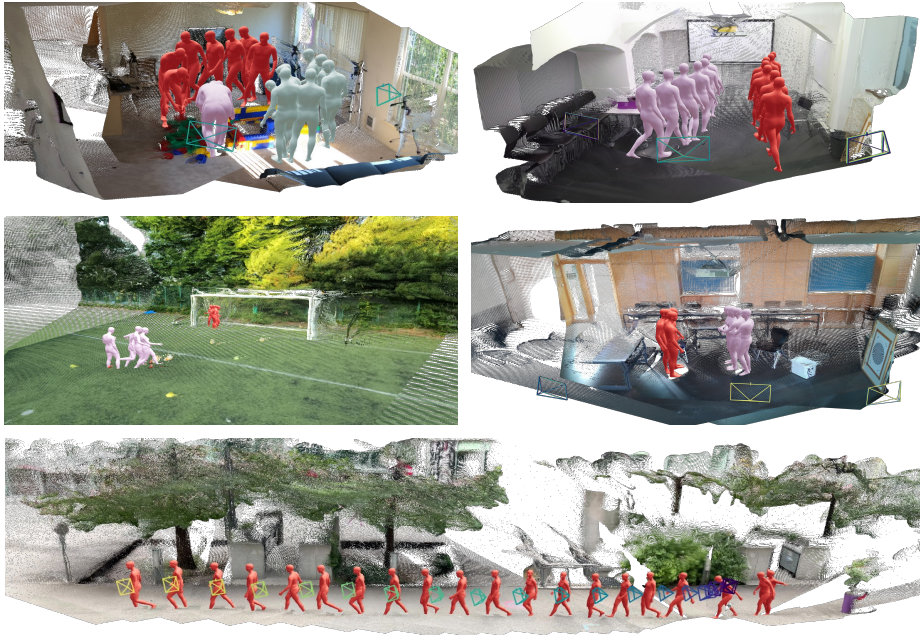


**Fig. 4:** Qualitative results on EgoBody, EgoHumans, EgoExo4D, and EMDB datasets.

construct an in-the-wild training set by combining 3DPW [46], MPII [2], and MSCOCO [28], and mix it with BEDLAM. We obtain 2D SMPL vertex and joint annotations of in-the-wild datasets using [32]. The second-stage objective comprises the pelvis detection loss and the 2D reprojection loss from stage 1, and the Chamfer distance loss that compares the visible SMPL vertices with the predicted masked depth map to enforce geometric consistency. Unlike stage 1, the scale factor  $s_{\text{opt}}$  is not applied in this stage due to the absence of ground-truth depth maps. Details about losses are provided in the supplement.

## 4 Experiments

### 4.1 Experimental Setup

We evaluate the CHROMM’s performance on two conventional tasks of (i) global human motion estimation and (ii) multi-view human pose estimation.

We measure global motion accuracy in the world coordinate system using three metrics. World-Aligned MPJPE (WA-MPJPE) aligns all predicted joints of all frames to the ground-truth using a Sim(3) transformation. World MPJPE (W-MPJPE) aligns using only the first two frames using Sim(3). Both metrics are reported in millimeters (mm). We also report the Root Translation Error (RTE, %), which measures the root translation error after SE(3) alignment (without scaling) over the entire sequence. The error is normalized by the total displacement to account for varying motion magnitudes. We conduct

**Table 1:** Quantitative comparison on EMDB-2 and RICH dataset. **red** : the best, **yellow** : the second best.

	Settings			EMDB-2			RICH		
	Multi-View	Multi-Person	No Extern.	WA-MPJPE↓	W-MPJPE↓	RTE(%)↓	WA-MPJPE↓	W-MPJPE↓	RTE(%)↓
JOSH3R [29]	✗	✓	✗	220.0	661.7	13.1	-	-	-
UniSH [25]	✗	✗	✗	118.5	270.1	5.8	118.1	183.2	4.8
Human3R [8]	✗	✓	✓	112.2	267.9	2.2	110.0	184.9	3.3
Ours-mono	✗	✓	✓	102.6	255.0	1.7	87.5	138.3	3.3
Ours-multi	✓	✓	✓	-	-	-	53.1	79.0	1.4

experiments on EMDB-2 [20] and RICH [19] dataset where EMDB-2 consists of monocular dynamic-camera videos, and RICH provides a fixed multi-view camera setup. Since EMDB-2 is monocular, we evaluate only the monocular setting. For RICH, we report results under both monocular and multi-view settings. We compare CHROMM with recent feed-forward monocular human-scene reconstruction models, including JOSH3R [29], UniSH [25], and Human3R [8].

To further assess multi-view performance, following prior work, we evaluate on EgoHumans [22] and EgoExo4D [17] under a single-frame setting. We report three metrics as follows. World MPJPE (W-MPJPE<sup>†</sup>) in this protocol measures joint errors in the world coordinate system after aligning only the camera poses using SE(3) alignment (without scaling). Group-Aligned MPJPE (GA-MPJPE) evaluates joint errors after applying a single Sim(3) transformation to all persons jointly within each frame, preserving inter-person spatial relationships. Procrustes-aligned MPJPE (PA-MPJPE) applies person-wise Procrustes alignment, measuring local pose accuracy independent of global position and scale. All metrics in this setting are reported in meters (m).

## 4.2 Global Human Motion Estimation

We compare our method with existing monocular feed-forward human-scene reconstruction models under both monocular and multi-view settings. Following prior protocol, we divide each sequence into 100-frame segments for monocular evaluation. For the multi-view setting, we use all available views. To avoid out-of-memory issues, we process sequences in 25-frame chunks and stitch them into 100-frame segments using Sim(3) alignment based on estimated camera poses.

JOSH3R is one of the earliest approaches to unify human-scene reconstruction, but it requires additional inputs such as 2D human masks. UniSH combines Pi3 and CameraHMR [34] with AlignNet, yet relies on bounding box detectors and operates in a single-person setting. Human3R removes external dependencies and supports multi-person reconstruction, but does not extend to multi-view scenarios. As shown in Table 1, our model achieves superior performance in both monocular and multi-view settings without relying on external modules.

## 4.3 Multi-View Human Pose Estimation

We further compare our method with existing multi-view human-scene reconstruction approaches. Since HSfM [33] and HAMSt3R [37] operate on a single-

**Table 2:** Quantitative comparison on EgoHumans and EgoExo4D dataset.

	Settings				EgoHumans			EgoExo4D	
	Video	No ReID	No Optim.	No Extern.	W-MPJPE $\dagger$	GA-MPJPE $\downarrow$	PA-MPJPE $\downarrow$	W-MPJPE $\dagger$	PA-MPJPE $\downarrow$
HSM(init.)	$\times$	$\times$	$\checkmark$	$\checkmark$	4.28	0.51	0.06	5.29	0.07
HSM [33]	$\times$	$\times$	$\times$	$\times$	1.04	0.21	0.05	0.56	0.06
HAMSt3R [37]	$\times$	$\checkmark$	$\triangle$	$\checkmark$	3.80	0.42	0.14	0.51	0.09
Ours	$\checkmark$	$\checkmark$	$\checkmark$	$\checkmark$	0.51	0.15	0.05	0.26	0.06

timestep basis, we adopt the same evaluation protocol for a fair comparison. Notably, while prior methods require ground-truth re-identification information, our model is evaluated without such supervision. As shown in Table 2, our method achieves competitive performance without relying on iterative optimization or external modules.

**Runtime Comparison.** We compare the total computation time between multi-view approaches. For fair comparison, we run inference on a single timestep with three people and four views scene in EgoHumans on a single NVIDIA V100 GPU. Our model does not require additional preprocessing stages or iterative optimization procedures, achieving over  $8\times$  speedup compared to HAMSt3R.

**Table 3:** Runtime comparison result.

	Method	Total Runtime $\downarrow$
Single	HSM	$\sim 118s$
	HAMSt3R	$\sim 32s$
	Ours	$\sim 4s$

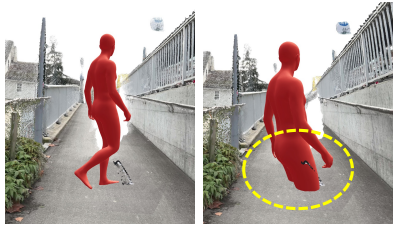
#### 4.4 Qualitative Result

We present additional qualitative results in Fig. 4. Given multi-person, multi-view video inputs, our model reconstructs coherent human meshes along with the surrounding scene in diverse settings. Our model operates robustly in multi-view and monocular inputs, single-person and multi-person scenarios, indoor and outdoor environments, demonstrating its effectiveness in real-world scenarios. More results with diverse settings are in the supplement.

#### 4.5 Ablation Studies

**Scale Adjustment.** We evaluate the effectiveness of the scale adjustment module on EMDB-2, which contains a wide range of scene scales. As shown in Table 4, relying solely on the scale predicted by Pi3X results leads to a performance drop due to the scale gap between the reconstructed scene and human meshes (Fig. 5). In contrast, enabling scale adjustment allows the model to adapt to diverse scene scales and achieve consistent performance across different scenarios.

**Multi-View Fusion.** We further evaluate different multi-view fusion strategies on the RICH dataset. As shown in Table 5, averaging per-view predictions, including the translation results, results in the lowest performance. Adopting triangulation (Tri.) instead of translation average yielded a performance gain.



(a) w/ scale adj. (b) w/o scale adj.

**Fig. 5:** Effect of scale adjustment.**Table 5:** Ablation on multi-view fusion strategies on RICH.

RICH	WA-M.↓	W-M.↓	RTE(%)↓
Only Avg.	69.3	105.7	1.7
Max-Pool+Tri.	63.2	90.1	<b>1.3</b>
Avg.+Tri.	<b>53.1</b>	<b>79.0</b>	1.4

**Table 4:** Ablation on scale adjustment on EMDB-2.

EMDB-2	WA-M.↓	W-M.↓	RTE(%)↓
w/o scale adj.	169.7	447.9	4.2
w/ scale adj.	<b>102.6</b>	<b>255.0</b>	<b>1.7</b>

**Table 6:** Ablation on multi-person association strategies on EgoHumans.

RICH	WA-M.↓	W-M.↓	RTE(%)↓	EgoHumans	Acc.(%)	Prec.(%)	Recall.(%)
Only Avg.	69.3	105.7	1.7	Pose	70.6	48.5	86.0
Max-Pool+Tri.	63.2	90.1	<b>1.3</b>	Position	91.1	<b>91.0</b>	75.7
Avg.+Tri.	<b>53.1</b>	<b>79.0</b>	1.4	Combined	<b>91.3</b>	90.9	<b>76.6</b>

Finally, compared to the implicit max-pooling strategy, explicitly averaging the predicted view-invariant parameters achieved the highest performance, demonstrating the importance of separating view-invariant attributes with the view-dependent attributes.

**Multi-Person Association.** We evaluate different matching strategies and report the re-identification (Re-ID) success rate in Table 6. We evaluate on the EgoHumans dataset. As reported in [33], appearance-based re-identification faces difficulties when appearance features become difficult to distinguish. In contrast, we use explicit geometric cues for identity matching. Using pose information alone yields relatively low matching accuracy. Using positional cues alone significantly improves performance. Finally, combining both pose and positional cues further boosts accuracy, particularly in challenging cases where positional information alone is insufficient. Also, using pose information alone results in the highest recall with the lowest precision indicating that individuals with similar poses are frequently over-matched.

## 5 Conclusion

In this paper, we present CHROMM, a unified framework that jointly reconstructs cameras, scene geometry, and multiple humans from multi-person multi-view video in a single pass without relying on external modules or preprocessing. We integrate strong geometric and motion priors from Pi3X and Multi-HMR, while addressing the scale discrepancy between them by using a head-pelvis ratio. We propose a test-time multi-view fusion method that aggregates per-view estimates into a single representation. Furthermore, we introduce a multi-human association method that leverages predicted poses and spatial position cues. Experiments show that our model achieves competitive performance in global hu-

man motion estimation and multi-view pose estimation while running over  $8\times$  faster than prior multi-view approaches.

**Limitations and Future Works.** Despite its effectiveness, CHROMM shares a common limitation with Multi-HMR and Human3R in that it heavily relies on head tokens. As a result, performance may degrade when the head region is severely occluded or not visible. We plan to extend the dual encoders into a integrated encoder design for both human and scene representation.

## References

1. Allshire, A., Choi, H., Zhang, J., McAllister, D., Zhang, A., Kim, C.M., Darrell, T., Abbeel, P., Malik, J., Kanazawa, A.: Visual imitation enables contextual humanoid control. In: Proceedings of the Conference on Robot Learning (CoRL) (2025)
2. Andriluka, M., Pishchulin, L., Gehler, P., Schiele, B.: 2d human pose estimation: New benchmark and state of the art analysis. In: Proceedings of the IEEE Conference on Computer Vision and Pattern Recognition. pp. 3686–3693 (2014)
3. Baradel, F., Armando, M., Galaaoui, S., Brégier, R., Weinzaepfel, P., Rogez, G., Lucas, T.: Multi-hmr: Multi-person whole-body human mesh recovery in a single shot. In: European Conference on Computer Vision. pp. 202–218. Springer (2024)
4. Beardsley, P., Torr, P., Zisserman, A.: 3d model acquisition from extended image sequences. In: European conference on computer vision. pp. 683–695. Springer (1996)
5. Black, M.J., Patel, P., Tesch, J., Yang, J.: Bedlam: A synthetic dataset of bodies exhibiting detailed lifelike animated motion. In: Proceedings of the IEEE/CVF Conference on Computer Vision and Pattern Recognition. pp. 8726–8737 (2023)
6. Cadena, C., Carlone, L., Carrillo, H., Latif, Y., Scaramuzza, D., Neira, J., Reid, I., Leonard, J.J.: Past, present, and future of simultaneous localization and mapping: Toward the robust-perception age. *IEEE Transactions on robotics* **32**(6), 1309–1332 (2017)
7. Caesar, H., Bankiti, V., Lang, A.H., Vora, S., Liong, V.E., Xu, Q., Krishnan, A., Pan, Y., Baldan, G., Beijbom, O.: nuscenes: A multimodal dataset for autonomous driving. In: Proceedings of the IEEE/CVF conference on computer vision and pattern recognition. pp. 11621–11631 (2020)
8. Chen, Y., Chen, X., Xue, Y., Chen, A., Xiu, Y., Pons-Moll, G.: Human3r: Everyone everywhere all at once. *International Conference on Learning Representations* (2026)
9. Chen, Z., Yang, J., Huang, J., de Lutio, R., Esturo, J.M., Ivanovic, B., Litany, O., Gojcic, Z., Fidler, S., Pavone, M., Song, L., Wang, Y.: Omnire: Omni urban scene reconstruction. In: The Thirteenth International Conference on Learning Representations (2025)
10. Cuturi, M.: Sinkhorn distances: Lightspeed computation of optimal transport. *Advances in neural information processing systems* **26** (2013)
11. Durrant-Whyte, H., Bailey, T.: Simultaneous localization and mapping: part i. *IEEE robotics & automation magazine* **13**(2), 99–110 (2006)
12. Fitzgibbon, A.W., Zisserman, A.: Automatic camera recovery for closed or open image sequences. In: European conference on computer vision. pp. 311–326. Springer (1998)

13. Furukawa, Y., Ponce, J.: Accurate, dense, and robust multiview stereopsis. *IEEE transactions on pattern analysis and machine intelligence* **32**(8), 1362–1376 (2009)
14. Gabriel, P., Marco, C.: Computational optimal transport with applications to data sciences. *Foundations and Trends® in Machine Learning* **11**(5-6), 355–607 (2019)
15. Geiger, A., Lenz, P., Urtasun, R.: Are we ready for autonomous driving? the kitti vision benchmark suite. In: 2012 IEEE conference on computer vision and pattern recognition. pp. 3354–3361. IEEE (2012)
16. Goel, S., Pavlakos, G., Rajasegaran, J., Kanazawa, A., Malik, J.: Humans in 4d: Reconstructing and tracking humans with transformers. In: Proceedings of the IEEE/CVF International Conference on Computer Vision. pp. 14783–14794 (2023)
17. Grauman, K., Westbury, A., Torresani, L., Kitani, K., Malik, J., Afouras, T., Ashutosh, K., Baiyya, V., Bansal, S., Boote, B., et al.: Ego-exo4d: Understanding skilled human activity from first-and third-person perspectives. In: Proceedings of the IEEE/CVF Conference on Computer Vision and Pattern Recognition. pp. 19383–19400 (2024)
18. Hassan, M., Choutas, V., Tzionas, D., Black, M.J.: Resolving 3d human pose ambiguities with 3d scene constraints. In: Proceedings of the IEEE/CVF international conference on computer vision. pp. 2282–2292 (2019)
19. Huang, C.H.P., Yi, H., Höschle, M., Safroshkin, M., Alexiadis, T., Polikovsky, S., Scharstein, D., Black, M.J.: Capturing and inferring dense full-body human-scene contact. In: Proceedings of the IEEE/CVF Conference on Computer Vision and Pattern Recognition. pp. 13274–13285 (2022)
20. Kaufmann, M., Song, J., Guo, C., Shen, K., Jiang, T., Tang, C., Zárata, J.J., Hilliges, O.: Emdb: The electromagnetic database of global 3d human pose and shape in the wild. In: Proceedings of the IEEE/CVF International Conference on Computer Vision. pp. 14632–14643 (2023)
21. Keetha, N., Müller, N., Schönberger, J., Porzi, L., Zhang, Y., Fischer, T., Knapitsch, A., Zauss, D., Weber, E., Antunes, N., Luiten, J., Lopez-Antequera, M., Bulò, S.R., Richardt, C., Ramanan, D., Scherer, S., Kotschieder, P.: MapAnything: Universal feed-forward metric 3D reconstruction. In: International Conference on 3D Vision (3DV). IEEE (2026)
22. Khirodkar, R., Bansal, A., Ma, L., Newcombe, R., Vo, M., Kitani, K.: Ego-humans: An ego-centric 3d multi-human benchmark. In: Proceedings of the IEEE/CVF International Conference on Computer Vision. pp. 19807–19819 (2023)
23. Kim, S., Do, S., Park, J.: Showmak3r: Compositional tv show reconstruction. In: Proceedings of the Computer Vision and Pattern Recognition Conference. pp. 864–874 (2025)
24. Leroy, V., Cabon, Y., Revaud, J.: Grounding image matching in 3d with mast3r. In: European conference on computer vision. pp. 71–91. Springer (2024)
25. Li, M., Li, P., Zhang, Z., Lu, J., Zhao, C., Xue, W., Liu, Q., Peng, S., Zhang, W., Luo, W., et al.: Unish: Unifying scene and human reconstruction in a feed-forward pass. *Proceedings IEEE Conf. on Computer Vision and Pattern Recognition (CVPR)* (2026)
26. Li, Y.J., Xu, Y., Khirodkar, R., Park, J., Kitani, K.: Multi-person 3d pose estimation from multi-view uncalibrated depth cameras. *arXiv preprint arXiv:2401.15616* (2024)
27. Lin, H., Chen, S., Liew, J., Chen, D.Y., Li, Z., Shi, G., Feng, J., Kang, B.: Depth anything 3: Recovering the visual space from any views. *arXiv preprint arXiv:2511.10647* (2025)

28. Lin, T.Y., Maire, M., Belongie, S., Hays, J., Perona, P., Ramanan, D., Dollár, P., Zitnick, C.L.: Microsoft coco: Common objects in context. In: European conference on computer vision. pp. 740–755. Springer (2014)
29. Liu, Z., Lin, J., Wu, W., Zhou, B.: Joint optimization for 4d human-scene reconstruction in the wild. Internatioanl Conference on Learning Representations (2026)
30. Longuet-Higgins, H.C.: A computer algorithm for reconstructing a scene from two projections. *Nature* **293**(5828), 133–135 (1981)
31. Loper, M., Mahmood, N., Romero, J., Pons-Moll, G., Black, M.J.: SMPL: A skinned multi-person linear model. *ACM Trans. Graphics (Proc. SIGGRAPH Asia)* **34**(6), 248:1–248:16 (Oct 2015)
32. Moon, G., Choi, H., Lee, K.M.: Neuralannot: Neural annotator for 3d human mesh training sets. In: Proceedings of the IEEE/CVF Conference on Computer Vision and Pattern Recognition. pp. 2299–2307 (2022)
33. Müller, L., Choi, H., Zhang, A., Yi, B., Malik, J., Kanazawa, A.: Reconstructing people, places, and cameras. In: Proceedings of the Computer Vision and Pattern Recognition Conference. pp. 21948–21958 (2025)
34. Patel, P., Black, M.J.: Camerahr: Aligning people with perspective. In: 2025 International Conference on 3D Vision (3DV). pp. 1562–1571. IEEE (2025)
35. Pavlakos, G., Choutas, V., Ghorbani, N., Bolkart, T., Osman, A.A.A., Tzionas, D., Black, M.J.: Expressive body capture: 3D hands, face, and body from a single image. In: Proceedings IEEE Conf. on Computer Vision and Pattern Recognition (CVPR). pp. 10975–10985 (2019)
36. Radianti, J., Majchrzak, T.A., Fromm, J., Wohlgenannt, I.: A systematic review of immersive virtual reality applications for higher education: Design elements, lessons learned, and research agenda. *Computers & education* **147**, 103778 (2020)
37. Rojas, S., Armando, M., Ghanem, B., Weinzaepfel, P., Leroy, V., Rogez, G.: Hamst3r: Human-aware multi-view stereo 3d reconstruction. In: Proceedings of the IEEE/CVF International Conference on Computer Vision. pp. 5027–5037 (2025)
38. Schonberger, J.L., Frahm, J.M.: Structure-from-motion revisited. In: Proceedings of the IEEE conference on computer vision and pattern recognition. pp. 4104–4113 (2016)
39. Schönberger, J.L., Zheng, E., Frahm, J.M., Pollefeys, M.: Pixelwise view selection for unstructured multi-view stereo. In: European conference on computer vision. pp. 501–518. Springer (2016)
40. Seitz, S.M., Curless, B., Diebel, J., Scharstein, D., Szeliski, R.: A comparison and evaluation of multi-view stereo reconstruction algorithms. In: 2006 IEEE computer society conference on computer vision and pattern recognition (CVPR'06). vol. 1, pp. 519–528. IEEE (2006)
41. Sereno, M., Wang, X., Besançon, L., McGuffin, M.J., Isenberg, T.: Collaborative work in augmented reality: A survey. *IEEE transactions on visualization and computer graphics* **28**(6), 2530–2549 (2020)
42. Shen, Z., Pi, H., Xia, Y., Cen, Z., Peng, S., Hu, Z., Bao, H., Hu, R., Zhou, X.: World-grounded human motion recovery via gravity-view coordinates. In: SIGGRAPH Asia 2024 Conference Papers. pp. 1–11 (2024)
43. Shin, S., Kim, J., Halilaj, E., Black, M.J.: Wham: Reconstructing world-grounded humans with accurate 3d motion. In: Proceedings of the IEEE/CVF Conference on Computer Vision and Pattern Recognition. pp. 2070–2080 (2024)
44. Sun, P., Kretschmar, H., Dotiwala, X., Chouard, A., Patnaik, V., Tsui, P., Guo, J., Zhou, Y., Chai, Y., Caine, B., et al.: Scalability in perception for autonomous driving: Waymo open dataset. In: Proceedings of the IEEE/CVF conference on computer vision and pattern recognition. pp. 2446–2454 (2020)

45. Tomasi, C., Kanade, T.: Shape and motion from image streams under orthography: a factorization method. *International journal of computer vision* **9**(2), 137–154 (1992)
46. Von Marcard, T., Henschel, R., Black, M.J., Rosenhahn, B., Pons-Moll, G.: Recovering accurate 3d human pose in the wild using imus and a moving camera. In: *Proceedings of the European conference on computer vision (ECCV)*. pp. 601–617 (2018)
47. Wang, J., Chen, M., Karaev, N., Vedaldi, A., Rupprecht, C., Novotny, D.: Vggt: Visual geometry grounded transformer. In: *Proceedings of the Computer Vision and Pattern Recognition Conference*. pp. 5294–5306 (2025)
48. Wang, Q., Zhang, Y., Holynski, A., Efros, A.A., Kanazawa, A.: Continuous 3d perception model with persistent state. In: *Proceedings of the Computer Vision and Pattern Recognition Conference*. pp. 10510–10522 (2025)
49. Wang, R., Xu, S., Dai, C., Xiang, J., Deng, Y., Tong, X., Yang, J.: Moge: Unlocking accurate monocular geometry estimation for open-domain images with optimal training supervision. In: *Proceedings of the IEEE/CVF Conference on Computer Vision and Pattern Recognition*. pp. 5261–5271 (2025)
50. Wang, S., Leroy, V., Cabon, Y., Chidlovskii, B., Revaud, J.: Dust3r: Geometric 3d vision made easy. In: *Proceedings of the IEEE/CVF conference on computer vision and pattern recognition*. pp. 20697–20709 (2024)
51. Wang, Y., Zhou, J., Zhu, H., Chang, W., Zhou, Y., Li, Z., Chen, J., Pang, J., Shen, C., He, T.:  $\pi^3$ : Permutation-equivariant visual geometry learning. *arXiv preprint arXiv:2507.13347* (2025)
52. Wang, Y., Wang, Z., Liu, L., Daniilidis, K.: Tram: Global trajectory and motion of 3d humans from in-the-wild videos. In: *European Conference on Computer Vision*. pp. 467–487. Springer (2024)
53. Yang, X., Kukreja, D., Pinkus, D., Sagar, A., Fan, T., Park, J., Shin, S., Cao, J., Liu, J., Ugrinovic, N., et al.: Sam 3d body: Robust full-body human mesh recovery. *arXiv preprint arXiv:2602.15989* (2026)
54. Ye, V., Pavlakos, G., Malik, J., Kanazawa, A.: Decoupling human and camera motion from videos in the wild. In: *Proceedings of the IEEE/CVF conference on computer vision and pattern recognition*. pp. 21222–21232 (2023)

# Appendix

This supplementary material contains the implementation details of our model, CHROMM, along with the additional experiments and results to support our claims. In Sec. A, we describe the training setup, loss design, and matching algorithm. Sec. B presents additional experiments on SMPL translation strategies, pelvis detection comparison with robustness analysis, two-stage training ablation, scene reconstruction performance, and inference time on multi-view video. Sec. C includes additional human–scene reconstruction results across diverse scenarios. Finally, in Sec. D, we present failure cases.

## A Implementation Details

In this section, we describe the implementation details of CHROMM, including the training setup, loss design, and matching algorithm.

**Training Details.** As mentioned in Sec. 3.4, we train the model in two stages. In Stage 1, we freeze the Pi3 [51] encoder and decoder, as well as the Multi-HMR [3] encoder, and train the SMPL decoders together with the fusion, mask, and pelvis detection MLPs. These modules are trained for 20 epochs. During the first 10 epochs, scale adjustment is disabled to focus on learning human shape, poses, and translations. After this warm-up phase, scale adjustment is enabled, and training continues for the remaining 10 epochs. For each training sample, the input sequence length is randomly sampled between 2 and 24 frames. We use the AdamW optimizer with a OneCycleLR scheduler, starting from a learning rate of  $5 \times 10^{-5}$ . During this stage, the ground-truth camera intrinsics and head keypoint locations are provided.

In Stage 2, we freeze all modules except the pelvis detection MLPs and train them for 10 epochs. In this stage, the model takes a single image as input, and only head keypoint locations are provided. We again use the AdamW optimizer with a OneCycleLR scheduler, starting from a learning rate of  $1 \times 10^{-4}$ . We set the maximum number of people per frame to 10. The model is trained using 4 NVIDIA A100 GPUs. Stage 1 and Stage 2 training each take approximately one day, resulting in a total training time of about two days.

**Loss Design.** In Stage 1, we train the model using three types of losses: geometric, parametric, and detection losses. The geometric losses supervise the SMPL vertices  $\mathcal{V}^{3D}$  and 3D joints  $\mathcal{J}^{3D}$  by comparing them with the ground-truth SMPL vertices  $\hat{\mathcal{V}}^{3D}$  and 3D joints  $\hat{\mathcal{J}}^{3D}$ , where each loss is denoted as  $\mathcal{L}_{v3d}, \mathcal{L}_{j3d}$ . As mentioned in Sec. 3.4, we apply scale factor  $s_{opt}$  derived with ROE solver [49] to estimated SMPL translation  $\tau$ , SMPL vertices  $\mathcal{V}^{3D}$  and 3D joints  $\mathcal{J}^{3D}$  for alignment with the ground-truth sample. We also compare the reprojected vertices  $\mathcal{V}^{2D}$  and 2D joints  $\mathcal{J}^{2D}$  to ground-truth reprojected vertices  $\hat{\mathcal{V}}^{2D}$  and 2D joints  $\hat{\mathcal{J}}^{2D}$ , where each loss is denoted as  $\mathcal{L}_{v2d}, \mathcal{L}_{j2d}$ . The parametric losses directly supervise the predicted SMPL parameters  $\theta^{full}, \beta, \tau$  with the ground-truth SMPL

parameters  $\hat{\theta}^{\text{full}}, \hat{\beta}, \hat{\tau}$ , where each loss is denoted as  $\mathcal{L}_{\theta^{\text{full}}}, \mathcal{L}_{\beta}, \mathcal{L}_{\tau}$  and  $\theta^{\text{full}}$  denotes the full SMPL pose with root rotation  $R$ . Finally, detection losses are used to train MLP modules including the head detection MLP, mask prediction MLP, and pelvis detection MLPs. These modules are supervised by comparing estimated human mask, head and pelvis keypoints to the ground-truth samples. We calculate the detection losses by using binary cross-entropy (BCE) loss, where each loss is denoted as  $\mathcal{L}_{\text{mask}}, \mathcal{L}_{\text{head}}, \mathcal{L}_{\text{pelvis}}$ . Stage 1 loss is defined as follows:

$$\begin{aligned} \mathcal{L}_{\text{stage1}} = & \lambda_{\text{v3d}}\mathcal{L}_{\text{v3d}} + \lambda_{\text{j3d}}\mathcal{L}_{\text{j3d}} + \lambda_{\text{v2d}}\mathcal{L}_{\text{v2d}} + \lambda_{\text{j2d}}\mathcal{L}_{\text{j2d}} \\ & + \lambda_{\theta^{\text{full}}}\mathcal{L}_{\theta^{\text{full}}} + \lambda_{\beta}\mathcal{L}_{\beta} + \lambda_{\tau}\mathcal{L}_{\tau} \\ & + \lambda_{\text{mask}}\mathcal{L}_{\text{mask}} + \lambda_{\text{head}}\mathcal{L}_{\text{head}} + \lambda_{\text{pelvis}}\mathcal{L}_{\text{pelvis}} \end{aligned} \quad (5)$$

where  $\lambda_{\text{v3d}}, \lambda_{\text{j3d}}$  is set to 5.0,  $\lambda_{\text{v2d}}, \lambda_{\text{j2d}}, \lambda_{\theta^{\text{full}}}, \lambda_{\beta}, \lambda_{\tau}, \lambda_{\text{mask}}, \lambda_{\text{pelvis}}$  to 1.0, and  $\lambda_{\text{head}}$  to 0.1.

In Stage 2, we train  $\text{MLP}_{\text{coarse}}$  and  $\text{MLP}_{\text{fine}}$  by using pelvis loss  $\mathcal{L}_{\text{pelvis}}$ , reprojection losses  $\mathcal{L}_{\text{j2d}}$  and  $\mathcal{L}_{\text{v2d}}$  from Stage 1, and Chamfer loss  $\mathcal{L}_{\text{chamfer}}$  to enforce geometric consistency. Since in-the-wild datasets do not provide ground-truth depth maps, Chamfer loss  $\mathcal{L}_{\text{chamfer}}$  is computed between the predicted depth map and the visible SMPL vertices without scale factor  $s_{\text{opt}}$  applied. Final Stage 2 loss is defined as follows:

$$\begin{aligned} \mathcal{L}_{\text{stage2}} = & \lambda_{\text{v2d}}\mathcal{L}_{\text{v2d}} + \lambda_{\text{j2d}}\mathcal{L}_{\text{j2d}} \\ & + \lambda_{\text{head}}\mathcal{L}_{\text{head}} + \lambda_{\text{pelvis}}\mathcal{L}_{\text{pelvis}} + \lambda_{\text{chamfer}}\mathcal{L}_{\text{chamfer}} \end{aligned} \quad (6)$$

where  $\lambda_{\text{pelvis}}$  is set to 5.0,  $\lambda_{\text{v2d}}, \lambda_{\text{j2d}}, \lambda_{\text{chamfer}}$  to 1.0, and  $\lambda_{\text{head}}$  to 0.1.

**Association Algorithm.** Next, we describe the detailed multi-person association algorithm in Alg. 1. Given human tokens  $Z^{\text{human}}$  and SMPL 3D joints  $\mathcal{J}^{3\text{D}}$ , we first track humans in each view using pairwise L2 distance between consecutive human tokens and filter outliers by calculating average 3D joints displacement. After per-view tracking, we associate each human tracklets across views using Eq. 4. Finally, global human identities are assigned as output.

## B Additional Experiments

In this section, we present additional experiments to support our design choices. First, we compare different strategies for estimating SMPL translation. Next, we evaluate pelvis detection accuracy by comparing a coarse-to-fine approach with a direct prediction method, and visualize prediction results under occlusions and frame crop. We further analyze the effect of human tokens on scene reconstruction quality by evaluating scene depth maps. In addition, we study the impact of the two-stage training scheme on global human pose estimation. Finally, we provide extended measurements of inference time for each module in a multi-person, multi-view video setting.

**Translation estimation.** To estimate the SMPL translation, we predict a depth residual from the estimated depth map and unproject using the predicted camera intrinsics  $K$ , as described in Eq. 1. This formulation leverages the strong

---

**Algorithm 1** Multi-Person Association

---

```

1: Input: Human tokens  $Z^{\text{human}}$ , SMPL 3D joints  $\mathcal{J}^{3D}$  for each human in each frame
2: Output: Global human IDs for each human in each frame
3:
4: 1. Per-View Tracking
5: for each view  $v = 1, \dots, V$  do
6:   Initialize human track IDs for all detections at  $t = 1$ 
7:   for frame  $t = 2, \dots, T$  do
8:     Compute pairwise L2 distance matrix  $\mathcal{D}$  between tokens at  $t - 1$  and  $t$ 
9:     Perform one-to-one matching with threshold  $\gamma_{\text{match}}$ 
10:    Assign new human track IDs to unmatched detections
11:   end for
12:   for each human tracklet  $m$  do
13:     for each frame  $t = 2, \dots, T$  do
14:       Compute mean joint displacement  $\Delta = \frac{1}{J} \sum_j \|\mathcal{J}_{t,j}^m - \mathcal{J}_{t-1,j}^m\|_2$ 
15:       if  $\Delta > \gamma_{\text{outlier}}$  then
16:         Remove frame  $t$  from human tracklet  $m$ 
17:       end if
18:     end for
19:   end for
20: end for
21:
22: 2. Cross-View Association
23: Compute mean camera center for each view
24: Construct view connectivity graph using k-NN
25: for each connected view pair  $(v_i, v_j)$  do
26:   for each human tracklet pair  $(a, b)$  do
27:     Compute matching cost  $\mathcal{C}(a, b)$  using Eq. 4
28:   end for
29:   Solve one-to-one assignment via Hungarian algorithm
30:   Retain matches with  $\mathcal{C} < \gamma_{\text{reid}}$ 
31: end for
32: Assign global human IDs

```

---

geometric prior of Pi3, making the estimation more stable than directly predicting the SMPL translation from scratch. To validate this design choice, we compare three alternative strategies: (i) directly predicting the SMPL translation, (ii) directly predicting the depth and unprojecting it with  $K$ , and (iii) our approach that predicts a depth residual given the estimated depth map. For a fair comparison, all variants are trained only up to Stage 1 and evaluated on the EMDB [20] dataset using global human pose metrics. As shown in Table 7, methods that more effectively leverage the geometric prior from Pi3 consistently achieve better performance.

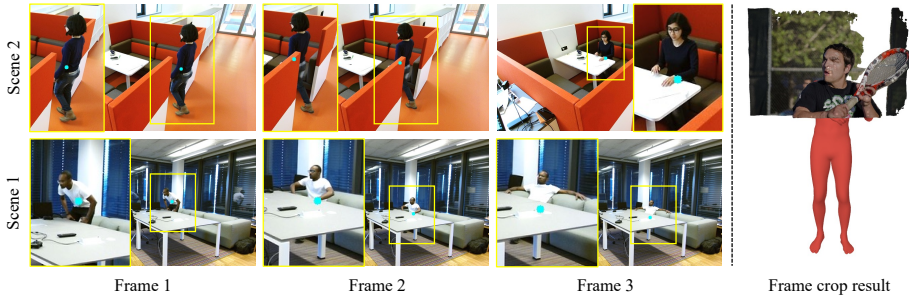
**Pelvis detection comparison.** We validate the effectiveness of our coarse-to-fine pelvis detection method on the 3DPW [46] test set by comparing the predicted pelvis keypoints to pseudo ground-truth annotations provided by [32],

**Table 7:** Ablation on different SMPL translation prediction strategies on EMDB-2.

Strategy	WA-M. ↓	W-M. ↓	RTE(%) ↓
Direct transl.	196.4	583.3	5.2
Direct depth	133.8	337.4	2.2
Depth residual	<b>107.5</b>	<b>265.9</b>	<b>1.7</b>

**Table 8:** Pelvis detection comparison on 3DPW.

Method	$e^{\text{pelvis}} \downarrow$
MLP <sub>coarse</sub>	0.0373
MLP <sub>fine</sub>	<b>0.0351</b>

**Fig. 6:** (Left) Pelvis detection visualization in occluded scenarios. Cyan dots denote the pelvis keypoints. (Right) Qualitative result on frame crop scenario.

since the original annotations are defined in COCO [28] format. We perform inference and evaluation per frame. We measure the pelvis localization error  $e^{\text{pelvis}}$ , defined as the L2 distance between the predicted and ground-truth pelvis keypoints normalized by the bounding box size as follows:

$$e^{\text{pelvis}} = \frac{\|p^{\text{pelvis}} - \hat{p}^{\text{pelvis}}\|_2}{\max(w_{\text{bbox}}, h_{\text{bbox}})}, \quad (7)$$

Here,  $p^{\text{pelvis}}$  and  $\hat{p}^{\text{pelvis}}$  denote the predicted and ground-truth pelvis locations, while  $w_{\text{bbox}}$  and  $h_{\text{bbox}}$  denote the width and height of the bounding box. As shown in Table 8, the proposed coarse-to-fine strategy achieves better accuracy than directly regressing the pelvis location from the head token.

**Pelvis detection robustness to occlusions.** Accurate pelvis localization is a key component for reliable scale adjustment. To analyze the effect of occlusion on pelvis detection, we visualize the predicted pelvis locations in scenes where the pelvis is occluded by surrounding objects. Interestingly, as illustrated in Fig. 6, our model is still able to estimate the pelvis location even under such occlusions. Furthermore, the final scale ratio is computed by averaging pelvis detections across all humans and frames, which makes the pelvis-based estimation robust to occasional occlusions. In cases where the pelvis keypoint falls outside the image boundary due to frame cropping, we instead use the coarse estimate predicted by MLP<sub>coarse</sub>, which also produces robust results.

**Early fusion impact on scene reconstruction.** Next, we analyze the effect of human tokens on scene reconstruction quality. We compare two strategies: (i) early fusion, where human tokens are jointly fed with patch tokens to the Pi3

**Table 9:** Scene depth comparison on PROX.

Method	AbsRel ↓	$\delta < 1.25$ ↑
Early fusion	0.0865	0.9029
Late fusion	<b>0.0857</b>	<b>0.9059</b>

**Table 10:** Ablation on two stage training on EMDB-2.

Stages	WA-M. ↓	W-M. ↓	RTE(%) ↓
Stage1	107.5	265.9	1.7
Stage2	<b>102.6</b>	<b>255.0</b>	<b>1.7</b>

decoder, and (ii) late fusion, where scene reconstruction is performed without interfering with the reconstruction process. To evaluate the impact on the original Pi3 performance, we measure single-view depth estimation on PROX [18] dataset, which provides ground-truth depth maps. We sample one frame every 100 frames and evaluate depth accuracy using Absolute Relative Error (Abs Rel) and thresholded accuracy ( $\delta < 1.25$ ). The predicted depth maps are aligned to the ground truth by adjusting the scale. For a fair comparison, all models are trained only up to Stage 1. To further ensure fairness, we assign zero positional embeddings to the human tokens in the early fusion setting, similar to the register tokens. As shown in Table 9, even with zero positional embeddings and frozen decoder weights, introducing additional tokens into the decoder input can still degrade scene reconstruction performance.

**Effect of two stage training.** We compare the global human pose estimation performance of CHROMM trained only on BEDLAM in Stage 1 with that of CHROMM further trained on in-the-wild datasets with pelvis prediction in Stage 2. As shown in Table 10, the two-stage training scheme improves performance by enabling more accurate scale adjustment.

**Inference time breakdown.** To further analyze the runtime cost of our model, we measure the computation time of each module in a multi-view video scenario, as shown in Table 11. We select a scene with three people and four views from EgoHumans and evaluate 25 timesteps per view, resulting in a total of 100 frames. We repeat the inference five times and report the average runtime on a single NVIDIA A100 GPU. Note that the feature fusion process includes encoding images into Multi-HMR features and estimating human masks, head and pelvis keypoints.

**Table 11:** Runtime analysis on multi-view video inference.

Module	Runtime ↓
Pi3 encoder	0.85s
Pi3 decoder	8.89s
Scene heads	1.72s
Feature fusion	2.89s
SMPL decoders	0.67s
Association	4.19s
Multi-View fusion	0.41s
Total	<b>19.63s</b>

## C Additional Results

In this section, we present additional qualitative results under various scenarios. As illustrated in Fig. 7, our model reconstructs humans and the scene in diverse multi-view settings. As shown in Fig. 8 and Fig. 9, our model can also handle monocular and single-image scenarios. To the best of our knowledge, CHROMM



Fig. 7: Qualitative results in multi-view settings.

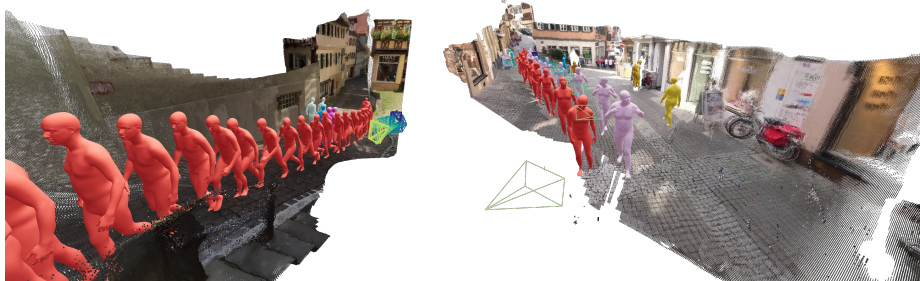


Fig. 8: Qualitative results in monocular settings.

is the first model capable of reconstructing both humans and the scene under both multi-view and monocular setups.

## D Limitations

In this section, we present failure cases where CHROMM fails to reconstruct humans and the scene. As shown in Fig. 10, our model exhibits limitations when handling complex poses and close human interactions. It also struggles when



Fig. 9: Qualitative results on single images.



Fig. 10: Failure cases.

the head is completely invisible in the image. Furthermore, the model faces challenges in extreme zoom-in scenarios where the head occupies most of the image. We leave these limitations for future work.